

# Optical and radiometric models of the NOMAD instrument part I: the UVIS channel

Ann C. Vandaele,<sup>1,\*</sup> Yannick Willame,<sup>1</sup> Cédric Depiesse,<sup>1</sup> Ian R. Thomas,<sup>1</sup> Séverine Robert,<sup>1</sup> David Bolsée,<sup>1</sup> Manish R. Patel,<sup>2,3</sup> Jon P. Mason,<sup>2</sup> Mark Leese,<sup>2</sup> Stefan Lesschaeve,<sup>4</sup> Philippe Antoine,<sup>5</sup> Frank Daerden,<sup>1</sup> Sofie Delanoye,<sup>1</sup> Rachel Drummond,<sup>1,6</sup> Eddy Neefs,<sup>1</sup> Bojan Ristic,<sup>1</sup> José-Juan Lopez-Moreno,<sup>7</sup> Giancarlo Bellucci,<sup>8</sup> and the NOMAD Team<sup>†</sup>

<sup>1</sup>Belgian Institute for Space Aeronomy (IASB-BIRA), 3 av Circulaire, 1180 Brussels, Belgium

<sup>2</sup>The Open University, Walton Hall, Milton Keynes, MK7 6AA, UK

<sup>3</sup>Space Science and Technology Department, STFC Rutherford Appleton Laboratory, Oxfordshire OX11 0QX, UK

<sup>4</sup>OIP, Westerring 21, 9700 Oudenaarde, Belgium

<sup>5</sup>LambdaX, Avenue Schuman 102, 1400 Nivelles, Belgium

<sup>6</sup>IndoSpace Ltd., 6 Nuneham Square, Abingdon, Oxon, OX14 1EH., UK

<sup>7</sup>Instituto de Astrofísica de Andalucía (IAA/CSIC), 18080 Granada, Spain

<sup>8</sup>Istituto di Astrofisica e Planetologia Spaziali (IAPS/INAF), 00133, Rome Italy

\*[a-c.vandaele@aeronomie.be](mailto:a-c.vandaele@aeronomie.be)

**Abstract:** The NOMAD instrument has been designed to best fulfil the science objectives of the ExoMars Trace Gas Orbiter mission that will be launched in 2016. The instrument is a combination of three channels that cover the UV, visible and IR spectral ranges and can perform solar occultation, nadir and limb observations. In this series of two papers, we present the optical models representing the three channels of the instrument and use them to determine signal to noise levels for different observation modes and Martian conditions. In this first part, we focus on the UVIS channel, which will sound the Martian atmosphere using nadir and solar occultation viewing modes, covering the 200-650nm spectral range. High SNR levels (>1000) can easily be reached for wavelengths higher than 300nm both in solar occultation and nadir modes when considering binning. Below 300nm SNR are lower primarily because of the lower signal and the impact of atmospheric absorption.

©2015 Optical Society of America

**OCIS codes:** (010.0280) Remote sensing and sensors; (120.6085) Space instrumentation; (120.6200) Spectrometers and spectroscopic instrumentation; (010.1280) Atmospheric composition; (010.5620) Radiative transfer.

---

## References and links

1. A. C. Vandaele, E. Neefs, R. Drummond, I. Thomas, F. Daerden, J.-J. Lopez-Moreno, M. Patel, G. Bellucci, M. Allen, F. Altieri, D. Bolsee, T. Clancy, E. Cloutis, S. Delanoye, C. Depiesse, E. Cloutis, A. Fedorova, V. Formisano, B. Funke, D. Fussen, A. Geminale, J.-C. Gérard, M. Giuranna, N. Ignatiev, J. Kaminski, O. Karatekin, F. Lefèvre, M. López-Puertas, M. López-Valverde, A. Mahieux, J. M. Connell, M. Mumma, L. Neary, E. Renotte, B. Ristic, S. Robert, M. Smith, S. Trokhimovsky, G. Villanueva, J. Whiteway, V. Wilquet, and M. Wolff, and the NOMAD Team, "Science objectives and performances of NOMAD, a spectrometer suite for the ExoMars TGO mission," *Planet. Space Sci.* in press.
2. E. Neefs, A. C. Vandaele, R. Drummond, I. R. Thomas, S. Berkenbosch, R. Clairquin, S. Delanoye, B. Ristic, J. Maes, S. Bonnewijn, G. Pieck, E. Equeter, C. Depiesse, F. Daerden, E. V. Ransbeeck, D. Nevejans, J. Rodriguez-Gómez, J.-J. López-Moreno, R. Sanz, R. Morales, G. P. Candini, M. C. Pastor-Morales, B. Aparicio Del Moral, J. M. Jeronimo-Zafra, J. M. Gómez-López, G. Alonso-Rodrigo, I. Pérez-Grande, J. Cubas, A. M. Gomez-Sanjuan, F. Navarro-Medina, T. Thibert, M. R. Patel, G. Bellucci, L. De Vos, S. Lesschaeve, N. V. Vooren, W. Moelans, L. Aballea, S. Glorieux, A. Baeke, D. Kendall, J. De Neef, A. Soenen, P. Y. Puech, J. Ward, J. F. Jamoye, D. Diez, A. Vicario-Arroyo, and M. Jankowski, "NOMAD spectrometer on the ExoMars trace gas orbiter mission: part 1—design, manufacturing and testing of the infrared channels," *Appl. Opt.* **54**(28), 8494–8520 (2015).
3. M. R. Patel, A. C. Vandaele, E. Neefs, and the NOMAD Team are preparing a manuscript to be called "NOMAD spectrometer on the ExoMars trace gas orbiter mission: part 2—design, manufacturing and testing of the UVIS channel," *Appl. Opt.* (in preparation).

4. V. Wilquet, R. Drummond, A. Mahieux, S. Robert, A. C. Vandaele, and J. L. Bertaux, "Optical extinction due to aerosols in the upper haze of Venus: Four years of SOIR/VEX observations from 2006 to 2010," *Icarus* **217**(2), 875–881 (2012).
5. V. Wilquet, A. Fedorova, D. Belyaev, M. Luginin, R. Drummond, A. Mahieux, S. Robert, A. C. Vandaele, F. Montmessin, and J.-L. Bertaux, "SPICAV/SOIR mesospheric aerosols observations and characterization," *Geophys. Res. Abstr.* **16**, 11491 (2014).
6. I.R. Thomas, A. C. Vandaele, S. Robert, E. Neefs, R. Drummond, F. Daerden, S. Delanoye, C. Depiesse, B. Ristic, A. Mahieux, L. Neary, Y. Willame, V. Wilquet, L. Aballea, W. Moelans, L. De Vos, S. Lesschaeve, N. Van Vooren, J. J. Lopez-Moreno, M. R. Patel, G. Bellucci, and the NOMAD Team, "Optical and radiometric models of the NOMAD instrument - Part II: The IR channels - SO and LNO," *Optics Express* (submitted for publication).
7. D. Nevejans, E. Neefs, E. Van Ransbeeck, S. Berkenbosch, R. Clairquin, L. De Vos, W. Moelans, S. Glorieux, A. Baeke, O. Korablev, I. Vinogradov, Y. Kalinnikov, B. Bach, J. P. Dubois, and E. Villard, "Compact high-resolution space-borne echelle grating spectrometer with AOTF based on order sorting for the infrared domain from 2.2 to 4.3 micrometer," *Appl. Opt.* **45**, 5191–5206 (2006).
8. A. C. Vandaele, M. De Mazière, R. Drummond, A. Mahieux, E. Neefs, V. Wilquet, O. Korablev, A. Fedorova, D. Belyaev, F. Montmessin, and J. L. Bertaux, "Composition of the Venus mesosphere measured by SOIR on board Venus Express," *J. Geophys. Res.* **113**, E00B23 (2008).
9. A. C. Vandaele, M. Kruglanski, and M. De Mazière, "Modeling and retrieval of Atmospheric spectra using ASIMUT" in *Proc. of the First Atmospheric Science Conference*, 2006).
10. R. Drummond, A. C. Vandaele, F. Daerden, D. Fussen, A. Mahieux, L. Neary, E. Neefs, S. Robert, Y. Willame, and V. Wilquet, "Studying methane and other trace species in the Mars atmosphere using a SOIR instrument," *Planet. Space Sci.* **59**(2-3), 292–298 (2011).
11. W. O. Gallery, F. X. Kneizys, and S. A. Clough, "Air mass computer program for atmospheric transmittance/radiance calculation: FSCATM," ERP-828/AFGL-TR-83-0065 (Air Force, 1983).
12. M. I. Mishchenko and L. D. Travis, "Capabilities and limitations of a current Fortran implementation of the T-matrix method for randomly oriented, rotationally symmetric scatterers," *J. Quant. Spectrosc. Radiat. Transf.* **60**(3), 309–324 (1998).
13. R. J. D. Spurr, "VLIDORT: A linearized pseudo-spherical vector discrete ordinate radiative transfer code for forward model and retrieval studies in multilayer multiple scattering media," *J. Quant. Spectrosc. Radiat. Transf.* **102**(2), 316–342 (2006).
14. S. Kochenova, M. De Mazière, A. C. Vandaele, T. Kerzenmacher, V. Letocart, N. Kumps, and Y. Willame, "ALVL 1.0: an advanced line-by-line radiative transfer model for the retrieval of atmospheric constituents from satellite and ground-based measurements," in *International Symposium "Atmospheric Radiation and Dynamics"*, 2011).
15. D. Bolsée, "Métrologie de la Spectrophotométrie Solaire Absolue: Principes, Mise en œuvre et Résultats. Instrument SOLSPEC à bord de la Station Spatiale Internationale," (Univ. Brussels, 2012).
16. D. Bolsée, N. Pereira, G. Cessateur, D. Gillotay, W. Peetermans, A. Michel, A. Sela, C. Jacobs, T. Foujols, S. Bekki, M. Marchand, A. Hauchecorne, M. Meftah, A. Irbah, and M. Hersé, "SOLAR/SOLSPEC mission on ISS: in-flight performances for SSI measurements in the UV," *Astron. Astrophys.* (in prep.).
17. F. Daerden, J. A. Whiteway, L. Neary, L. Komguem, M. T. Lemmon, N. G. Heavens, B. Cantor, E. Hébrard, and M. D. Smith, "A Solar Escalator on Mars: Self-Lifting of Dust Layers by Radiative Heating," *Geophys. Res. Lett.* **42**(18), 7319–7326 (2015).
18. B. Hapke, "Bidirectional reflectance spectroscopy 7: The single particle phase function hockey stick relation," *Icarus* **221**(2), 1079–1083 (2012).
19. M. J. Wolff, R. T. Clancy, J. D. Goguen, M. C. Malin, and B. A. Cantor, "Ultraviolet dust aerosol properties as observed by MARCI," *Icarus* **208**(1), 143–155 (2010).
20. M. G. Tomasko, L. Doose, M. Lemmon, P. H. Smith, and E. Wegryn, "Properties of dust in the Martian atmosphere from the Imager on Mars Pathfinder," *J. Geophys. Res.* **104**(E4), 8987–9008 (1999).
21. Y. Willame, A. C. Vandaele, C. Depiesse, D. Gillotay, S. Kochenova, and F. Montmessin, "Preliminary results of aerosols' properties studied with EPF measurements from the SPICAM/UV instrument," in *39th COSPAR Scientific Assembly*, 2012).
22. Y. Willame, A. C. Vandaele, D. Gillotay, C. Depiesse, R. Drummond, and F. Montmessin, "Studying the Martian aerosols UV properties with SPICAM," in *EGU General Assembly 2010*, 2010).
23. Y. Willame, "Aerosol and ozone retrieval in the Martian atmosphere using the SPICAM/UV instrument and preparation for future missions," (Univ. Libre de Bruxelles, Brussels, Belgium, 2015).
24. M. E. Ockert-Bell, J. B. Bell JF 3rd, C. P. Pollack, McKay, and F. Forget, "Absorption and scattering properties of the Martian dust in the solar wavelengths," *J. Geophys. Res.* **102**(E4), 9039–9050 (1997).

---

## 1. Introduction

NOMAD (Nadir and Occultation for MArs Discovery) is one of four instruments on board the ExoMars Trace Gas Orbiter [1], scheduled for launch in January 2016 and to begin nominal science mission around Mars in late 2017. It consists of a suite of three high-resolution spectrometers [2, 3] – UVIS (Ultraviolet-Visible), SO (Solar Occultation) and LNO (Limb

Nadir and Occultation) – which will generate a huge data set of Martian atmospheric observations during the mission, across a wide spectral range.

The SO spectrometer channel will perform occultation measurements, operating between 2.2 and 4.3 $\mu\text{m}$  at a resolution of  $\sim 0.15\text{cm}^{-1}$ , with 180 to 1000m vertical spatial sampling. LNO will perform limb scanning, nadir and occultation measurements, operating between 2.2 and 3.8 $\mu\text{m}$  at a resolution of  $\sim 0.3\text{cm}^{-1}$ . In nadir, global coverage will extend between  $\pm 74^\circ$  latitude with an Instantaneous Field of View (IFOV) of 0.5x17km on the surface. This channel can also make occultation measurements should the SO channel fail. UVIS will make limb, nadir and occultation measurements between 200 and 650nm, at a resolution of 1.5nm. It will achieve 300m vertical sampling with a 1km vertical resolution during occultation and 5x60km ground resolution during 15s nadir observations (IFOV of 5x5km).

An order-of-magnitude increase in spectral resolution over previous instruments will allow NOMAD to map previously unresolvable gas species, such as important trace gases and isotopes. CO, CO<sub>2</sub>, H<sub>2</sub>O, C<sub>2</sub>H<sub>2</sub>, C<sub>2</sub>H<sub>4</sub>, C<sub>2</sub>H<sub>6</sub>, H<sub>2</sub>CO, CH<sub>4</sub>, SO<sub>2</sub>, H<sub>2</sub>S, HCl, O<sub>3</sub> and several isotopologues of methane and water will be detectable, providing crucial measurements of the Martian D/H ratios. It will also be possible to map the sources and sinks of these gases, such as regions of surface volcanism/outgassing and atmospheric production, over the course of an entire Martian year, to further constrain atmospheric dynamics and climatology. NOMAD will also continue to monitor the Martian water, carbon, ozone and dust cycles, extending existing data sets made by successive space missions in the past decades, from which surface UV radiation levels will be determined. Using SO and LNO in combination with UVIS, aerosol properties such as optical depth, composition and size distribution can be derived for atmospheric particles and for distinguishing dust from ice aerosols, as demonstrated on Venus by the analysis of the SPICAV-UV, IR and SOIR data [4, 5].

The radiometric model of an instrument is critical for the accurate understanding of its characteristics and to correctly predict its expected performance. The analysis is based on the knowledge of the incoming radiation and of the transmittance or the reflectance of each of the elements of the instrument. Such a model consists in general of two elements: (1) the computation of the detected signal, considering the incoming radiation and the attenuation due to the different optical components; (2) the estimation of the noise on the detector. From these quantities signal to noise ratios (SNR) can be calculated and used further to investigate the sensitivity of the instruments.

The three channels of the NOMAD instrument and their science objectives will be briefly described in the next section. Then their radiometric and optical models will be detailed. In this paper we will focus on the UVIS channel model, while in the companion paper [6], the models and results for the IR channels will be presented and discussed.

## 2. The NOMAD instrument

NOMAD, the “Nadir and Occultation for MArs Discovery” spectrometer suite [1–3] was selected as part of the payload of the ExoMars Trace Gas Orbiter mission 2016. The instrument will conduct a spectroscopic survey of the Martian atmosphere in UV, visible and IR wavelengths covering the 0.2-0.65 and 2.3-4.3  $\mu\text{m}$  spectral ranges. NOMAD is composed of 3 channels: a solar occultation channel (SO) operating in the infrared wavelength domain, a second infrared channel capable of doing nadir, but also solar occultation and limb observations (LNO) and an ultraviolet/visible channel (UVIS) that can work in all observation modes. The spectral resolution of SO and LNO surpasses previous surveys in the infrared by more than one order of magnitude. NOMAD offers an integrated instrument combination of a flight-proven concept and innovations based on existing and proven instrumentation: SO is a copy of SOIR on Venus Express [7, 8] while LNO is an upgrade version of the same instrument and UVIS has heritage from the ExoMars lander. These 3 channels will provide mapping and vertical profile information at high spatio-temporal resolution.

The science objectives of the instrument are threefold [1]:

- (1) **Chemical Composition** - Analyse the present-day chemical composition of the Martian atmosphere through detection of a broad suite of trace gases and key isotopes. Extend the detection to the upper atmosphere in order to constrain atmospheric escape processes relating the present-day atmosphere to its past and future evolution. Understand the chemistry in order to constrain the methane origin (i.e. geophysical, exogenous or biological) and destruction processes, and study gases related to possible ongoing geophysical and volcanic activity on Mars.
- (2) **Climatology and Seasonal Cycles** - Characterize the spatial (3D) and temporal variability of trace gases; provide an extension and refinement of current climatologies for CO<sub>2</sub>, H<sub>2</sub>O, CO, CH<sub>4</sub>, O<sub>3</sub> and other species including and related UV radiation levels at the surface. Contribute to the understanding of fine-scale processes and annual variability, and to the constraint of atmospheric dynamics.
- (3) **Sources and Sinks** - Characterize the production and loss mechanisms of trace gases, including the localization of sources related to outgassing as well as atmospheric production. Refine processes in the water, carbon, ozone and dust cycles. Relate these to surface mineralogy/polar ices and characterize sites of interest.

**Table 1. NOMAD-UVIS characteristics and performances**

Characteristics	Solar occultation	Nadir
Volume	128mm x 152mm x 89mm	
Mass	950g	
Spectral range	200-650nm	
Spectral resolution	1.5nm	
Numerical aperture of the fiber	0.22	
F-number	2.15	2.18
FOV	2 arcmin	43 arcmin
IFOV	1km	5km x 5km
Typical observatio		
Binning	8 rows	64 rows
Observation time	0.2s	15s
Footprint of nadir channel		
during a typical 15s observation		60 km x 5km
Vertical sampling	< 300 m ( $\Delta z$ at limb)	
SNR (Specification requirement)	230-450nm: SNR $\geq$ 1000 450-650nm: SNR $\geq$ 500	230-450nm: SNR $\geq$ 500 450-650nm: SNR $\geq$ 250
<b>Detector</b> e2V back-thinned CCD30-11	2D 1024x256 pixel CCD	
Pixel pitch	26 $\mu$ m	
Dark current at 293K	1000 e-/pixel/s	
Dark signal non uniformity on binned column of 256 pixels at 293K	30 e-/pixel/s	
Read-out noise	6 e-/pixel	
Detector Full well capacity (at 293K)	540 000 e-	

The full description of the UV and IR channels can be found in [3] and [2] respectively. Here we will only briefly describe the UVIS channel. UVIS operates in the wavelength domain between 200 and 650nm. The spectrometer is a full copy of the instrument designed for the ExoMars lander, with two additional telescopes, one for each viewing channel. The spectrometer is based on the conventional Czerny-Turner configuration. The main components (see Fig. 1) are the entrance slit (Slit), the aperture (A), the collimating mirror (M1), the diffraction grating (G), the focusing mirror (M2), the 2nd order filter (F) and the detector (CCD). The light is delivered by an optical fibre. The spectrometer configuration combines simplicity and high-performances. In particular, the spectral range is very broad

(200-650nm) with optimized performance in the UV range. Blaze angle and incidence angle achieve the highest reflectance of the first diffraction order at 220nm. The 2nd order filter solves the issue of the overlap between the 1st diffraction order and the 2nd diffraction order of the grating. Indeed, due to the wide spectral range of the observed signal, first diffraction order rays and second diffraction order rays overlap on the detector. Hence a long-pass filter has been placed in front of the detector to block the second order contribution. The cutoff is chosen at 340nm. The filter is a window partially coated. The 2nd order signal goes through the coated area (see Fig. 2). As such the 2nd order signal is completely blocked as long as the signal at wavelength shorter than the wavelength corresponding to the uncoated-coated transition of the filter ( $\lambda_c$  in Fig. 2). The slit width is 65 $\mu$ m which corresponds to a resolution better than 1.5nm. This width results from a trade-off between resolution and the SNR. Table 1 summarizes the characteristics of the UVIS channel.

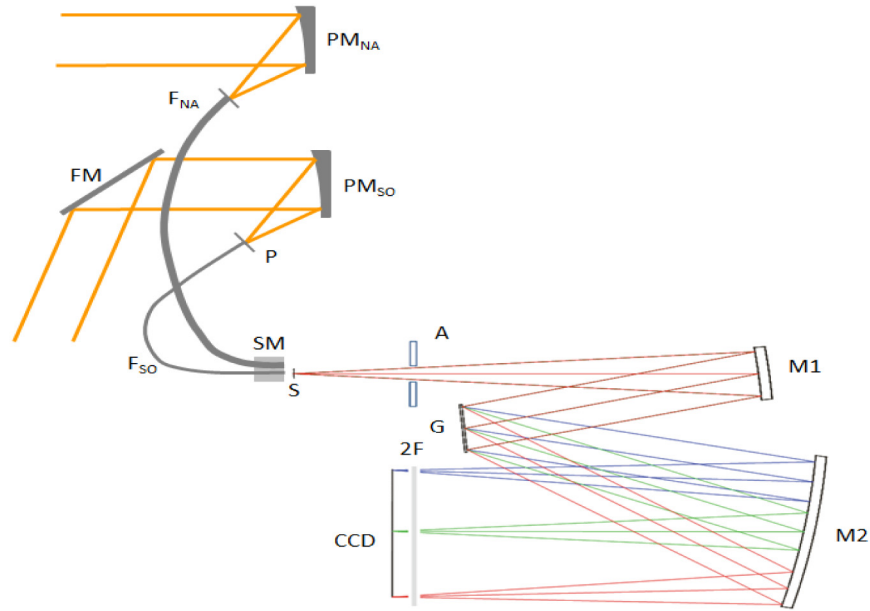


Fig. 1. Schematics of the UVIS instrument: the entrance optics for nadir observations (NA) with the parabolic mirror ( $PM_{NA}$ ) and the bundle of fibres ( $F_{NA}$ ), the entrance optics for solar occultation observations (SO) with the flat mirror (FM) located in the periscope, the parabolic mirror ( $PM_{SO}$ ), the pinhole (P) and the optical fibre ( $F_{SO}$ ); the selector mechanism (SM); the spectrometer with the entrance slit (S), the aperture (A), the collimating mirror (M1), the diffraction grating (G), the focusing mirror (M2), the 2nd order filter (2F) and the detector (CCD).

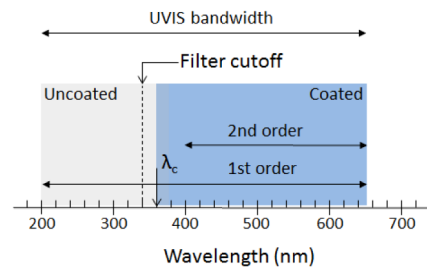


Fig. 2. Principle of the 2nd order filter. The wavelength scale refers to the positions of the 1st order signal on the filter as a function of the wavelength.  $\lambda_c$  is the wavelength corresponding to the uncoated-coated transition

Each telescope includes a single parabolic mirror for space and weight minimization. Light is focused on a single fibre and a bundle of fibres for the solar occultation channel and the nadir channel respectively. The field of views (2 arcmin for solar occultation and 43 arcmin for nadir) are determined by the focal length of the mirror and the entrance aperture of the fibre(s).

UVIS has one periscope in front of the solar telescope with a mirror allowing the pointing towards the Sun and a cut out hole in the NOMAD cover for the nadir viewing telescope (see [2] for more details). UVIS switches between nadir and solar viewing angles by alternating which optic fibre cable is placed at the input of the spectrometer. The selector mechanism is a rotating motor mechanism qualified on several space missions that moves the fibres in front of the slit. Fibre positioning is accurately defined by two hard stops.

### 3. Radiometric models

Building the radiometric model of an instrument is an essential step in the understanding of its characteristics and performances. Such a model must accurately represent each optical element of the instrument to assess the recorded signal knowing the level of incoming radiation, taking into account the attenuation introduced by all its components.

The incoming signal during solar occultations is directly given by the spectral radiance of the Sun attenuated by the transmission along the Line of Sight (LOS). For nadir observations however the incoming radiation consists of several terms: the radiation emitted by the planet itself (blackbody corresponding to the surface temperature), the contribution of the Sun radiation reflected by the planet's surface, the emission from the atmosphere itself and the scattering occurring within the atmosphere, which is an important contribution in the UV spectral range. None of the three channels of NOMAD are sensitive to the contribution due to the emission from the planet: only SO covers the spectral region where this contribution starts to be non-negligible with respect to the Sun contribution (at wavelengths  $> 4.0\mu\text{m}$ ), but this channel will never perform observation in nadir viewing geometry.

All radiances have been calculated using the ASIMUT-ALVL radiative code developed at IASB-BIRA [9]. Initially developed for Earth observation missions, the code was later adapted for planetary atmospheres, in particular for Venus [8] and Mars [10]. ASIMUT-ALVL is a modular program for radiative transfer calculations in planetary atmospheres. This code has been developed with the objective to be as general as possible, accepting different instrument types (Fourier Transform Spectrometers, grating spectrometers, AOTF combined with an echelle grating) and different geometries (nadir, ground-based, solar occultation/limb). The different radiation contributions such as the Sun contribution (direct or reflected on the surface), the surface emission contribution and the thermal atmospheric emission contribution are taken into account. The spectra can be simulated in the IR and in the UV as well. The surface is considered by default to be Lambertian, but a more complex treatment is possible as well (see section 4.2). The determination of the radiation path through the atmosphere, i.e. the path followed by the radiation reaching the instrument, requires that the planet's curvature and refraction be taken into account. The model is based on the ray-tracing program FSCATM [11]. ASIMUT-ALVL has been coupled to SPHER/TMATRIX [12] and LIDORT [13] codes [14] to include the complete treatment of the scattering effects into the radiative transfer calculations. Aerosols are included in the ASIMUT-ALVL code, either as extinction (ASIMUT) or full scattering species (ALVL, through the call to LIDORT).

The radiances are then injected into the models of the channels which determine the radiation transmitted through the instrument in order to estimate the signal received at the detector. Then the different sources of noise are evaluated, and the SNRs corresponding to the injected signals are computed.

In the following, we will first describe the details of the instrument models of the UVIS channel and the effect of all their optical elements, as well as the different sources of noise. This will be done for a series of scenarios in which the Mars-Sun distance, the surface albedo

of Mars, the solar zenith angle, and the dust content are changed. These scenarios are thought to be representative of the conditions that will be observed during the course of the mission.

### 3.1 Radiometric model of the UVIS Channel

Here we describe in detail the radiometric model of the UVIS channel, including the attenuation due to the entrance telescopes and other optical elements. SNR will be derived for the two viewing geometries, i.e. solar occultation and nadir observations.

The spectral radiant flux  $\Phi_\lambda$  [W.nm<sup>-1</sup>] through the optics is expressed as

$$\Phi_\lambda = L_\lambda \cdot \Omega_s \cdot S_s. \quad (1)$$

where  $L_\lambda$ ,  $S_s$  and  $\Omega_s$  are the source radiance [W.m<sup>-2</sup>sr<sup>-1</sup>.nm<sup>-1</sup>], the spectral radiant surface and the solid angle sustained by the optics respectively. If  $D$  is the input diameter of the telescope (see Fig. 1) then  $\Phi_\lambda$  can be written as

$$\Phi_\lambda = L_\lambda \cdot \left(\frac{\pi}{2}\right)^2 \cdot D^2 \cdot \sin^2\left(\frac{FOV}{2}\right). \quad (2)$$

where  $FOV$  is the angular field of view. The fibre diameter  $d$  is related to the F-number of the channel ( $F_\#$ ) by:

$$d = 2DF_\# \cdot \sin\left(\frac{FOV}{2}\right). \quad (3)$$

Finally, the spectral radiant flux  $\Phi_\lambda$  at the input of the fibre, is thus completely defined by the emitter radiance and the parameters of the fibre,

$$\Phi_\lambda = L_\lambda \left(\frac{\pi}{2}\right)^2 \frac{d^2}{4F_\#^2}. \quad (4)$$

Equation (4) is nothing else than the law of the conservation of the etendue of the light source,

$$S_s \Omega_s = S_f \Omega_f. \quad (5)$$

where  $S_f$  and  $\Omega_f$  are the fibre input surface and the solid angle defined by the numerical aperture of the fibre.

Taking into account the spectral dispersion and the integration time ( $\Delta t$ ), the number of photons collected by a column  $i$  of pixels is then computed by dividing the received energy by the photon energy. Finally, introducing the quantum efficiency of the sensor, the number of electrons  $S(i)$  accumulated over a column of pixels that corresponds to a particular wavelength  $\lambda_i$  is computed as

$$S(i) = QE(\lambda_i) A(\lambda_i) \frac{\Phi_\lambda}{hc / \lambda_i} \left(\frac{dx}{d\lambda}\right)_\lambda^{-1} \Delta x \Delta t. \quad (6)$$

where

- $QE(\lambda_i)$  is the CCD spectral quantum efficiency;
- $A(\lambda_i)$  is the wavelength dependent total attenuation of the instrument. It includes all the effects that are listed in the next section;
- $\left(\frac{dx}{d\lambda}\right)_\lambda$  is the spectrometer dispersion at wavelength  $\lambda$  [m.nm<sup>-1</sup>];
- $\Delta x$  is the pixel width [m].

The sources of noise (in electrons) are:

- The **dark current** (DC), which is calculated from the datasheet of the e2v CCD (1000 e<sup>-</sup>/pixel/s at 293 K) considering its dependence on temperature. Dark current level is high for some of the observation modes that will be used by the UVIS channel and might reach the same level as the signal especially in the 200-250nm region. The analysis method will rely on the accurate removal of the dark current, based on calibration measurements performed in the laboratory and also continuously monitored in-flight. Indeed specific observations are foreseen to monitor the dark current by looking at the dark space [1]. There is indeed no masked part on the detector or in the FOV to measure the dark current levels. The dark current measurements will consist in pointing the boresights towards dark sky to be sure that no light source lies within the FOV. Such observations will allow us to investigate the evolution of the dark current and its dependence to temperature. Note, however, that during Mars observations, dark frames will be obtained by placing the selector at the entrance of the UVIS channel in its 'dark' position ensuring that no light enters the spectrometer. Such dark frames will be recorded sequentially to any atmospheric measurement, and will directly be subtracted from the latter. This will ensure a total subtraction of the dark signal corresponding to the same recording conditions, i.e. binning, integration time and temperature.

For an integration time  $\Delta t$ , a binning over a column of  $npixels$ , the dark current can be obtained using:

$$DC = DC_{\text{pixel/s}} \cdot npixels \cdot \Delta t. \quad (7)$$

The dark current noise is estimated as the square root of the dark current:

$$N_{\text{dark}} = \sqrt{DC}. \quad (8)$$

- The **shot noise** evaluated as the square root of the signal ( $N_{\text{shot}} = \sqrt{S}$ );
- The **read-out noise**:  $N_{ro}$  (6 e<sup>-</sup>/pixel from the e2v CCD datasheet);
- The residual second order signal after the second order filter  $N_{2nd}$ .

Since we do not make any assumption on the randomness and independence of the noise sources the total noise is not the sum in quadrature of all terms but:

$$N(i) = N_{\text{shot}} + N_{\text{dark}} + N_{ro} + N_{2nd} = \sqrt{S} + \sqrt{DC} + N_{ro} + N_{2nd}. \quad (9)$$

considering that all noise sources add. If the considered sources are uncorrelated, the total noise computed using Eq. (9) will be an overestimate of the true noise value. The signal-to-noise ratio  $SNR$  at pixel  $i$  is computed using the following relation:

$$SNR(i) = \frac{S(i)}{N(i)}. \quad (10)$$

It is also useful to introduce the Noise Equivalent Spectral Radiance (NESR) which is defined as the minimum detectable radiance, i.e. the change in the input radiance that produces a change in signal equal to the noise ( $SNR = 1$ ). In the following we will determine the NESR for the typical observation conditions described in Table 1 for solar occultation and nadir geometries. NESR has been calculated using the following equation:

$$NESR(i) = \frac{N(i)}{\Re(i)}. \quad (11)$$

where  $\mathfrak{R}(i)$  represents the radiance response of the instrument and combines the effect of all optical elements of the instrument which will be described in the following. NESR and the radiance responsivity are plotted in Fig. 3 for both solar occultation and nadir typical observations (see Table 1). Two NESRs are shown for each observation mode, corresponding to  $N(i)$  including or not the shot noise which is directly linked to the input radiation level. Typical radiation levels have been selected for this plot: for solar occultation, radiation at the top of atmosphere, and for nadir, the radiation corresponding to a bright spot on Mars at aphelion ( $\text{sza} = 45^\circ$ , low aerosol loading), see next sections for a detailed description of these cases.

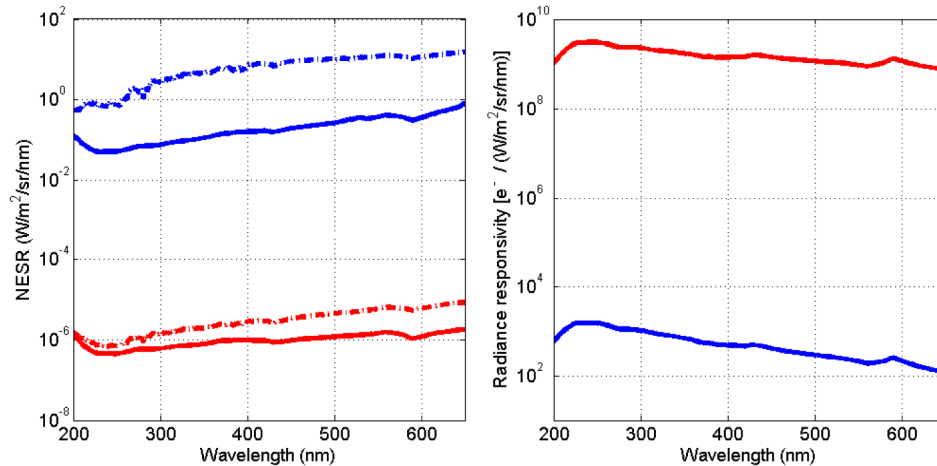


Fig. 3. Noise Equivalent Spectral Radiance (NESR, Left) and sensitivity (Right) for both observation modes considering the typical conditions for solar occultation (blue) and nadir (red) observations described in Table 1. NESRs calculated when considering all sources of noise including shotnoise are in dotted lines, whereas the NESRs without inclusion of the shotnoise are plotted in solid lines. The latter represent the noise due only to the instrument.

### 3.2 Optical elements of UVIS

The radiance responsivity includes all attenuations due to the instrument. In the following we will consider the different optical components of the UVIS channel that have an influence on the radiation level reaching the detector. A number of factors introduce losses from the front-end of the telescope to the detector. They are listed hereafter.

- The **telescope reflectivity** – For the collecting mirror of the nadir telescope ( $PM_{NA}$  in Fig. 1), the wavelength dependent reflectivity has been measured by the company which applied the coating on the mirror. For the solar occultation telescope, it has been computed from the refractive index of the material since there is no coating on the mirror to attenuate the signal.
- The **optical fibre** attenuation, which has been inferred directly from the fibre datasheet (SEDI- ATI Fibres Optiques, <http://www.sedi-fibres.com/>).
- The **slit area-to-fibre area ratio** – The attenuation is given by the geometrical factor which depends on the distance between the fibre and the slit, the width of the slit and the angular distribution of light coming out of the fibre. The angular distribution out of the fiber is peaked in the forward direction. The exact profile is complex for a multimode fibre since it depends on the distance from the fiber tip, for example. A simple Gaussian distribution is used in the simulation.
- The **spectrometer angular acceptance** which is limited by the size of the optics in general and of the first spherical mirror in particular. This is a geometrical factor

which depends on the distance between the slit and the mirror, the size and the shape of the mirror, and the angular distribution of light coming out of the fibre. It is moreover assumed that no other geometrical loss occurs afterwards.

- The **grating diffraction efficiency** (wavelength-dependent) – The first diffraction order defines the actual signal level. The second order contribution is included into the noise. Polarization effects of the grating are also taken into account.
- The **reflectivity of the two mirrors of the spectrometer** has been measured by the company (Schott) which applied the coating on the mirrors.
- The **second order filter transmission** (wavelength-dependent) – Data have been inferred from the technical datasheet of the filter.

## 4. Results

### 4.1 Solar occultation observations

For solar occultation, the incoming light is the solar radiance attenuated by the absorption by the atmosphere along the LOS which is defined from the centre of the Sun to the aperture of the instrument. For the Sun irradiance, we have used data obtained with the SOLSPEC instrument on board the International Space Station [15, 16]. For this sensitivity exercise, we have considered data corresponding to a quiet Sun, resulting for a large number of observations performed during the inter-cycles 23 to 24. The solar radiances, derived from the SOLSPEC irradiance taking into account the Mars-Earth distance and used as input for the model are shown in Fig. 4. They correspond to the radiance observed at the top of the atmosphere, and at the tangent heights of 65, 50, 20 and 10km respectively. Simulations have been performed considering a reference atmosphere based on the latest observations of the atmosphere composition. The core of this reference atmosphere are vertical profiles provided by the GEM-Mars GCM developed at IASB-BIRA [17]. Global annual profiles for the temperature, pressure, CO<sub>2</sub>, H<sub>2</sub>O, O<sub>3</sub> as well as dust extinction are given from the surface up to 130km. The impact of the CO<sub>2</sub> absorption at lower wavelengths is clearly seen in Fig. 4, as well as the typical O<sub>3</sub> absorption signature between 220 and 300nm.

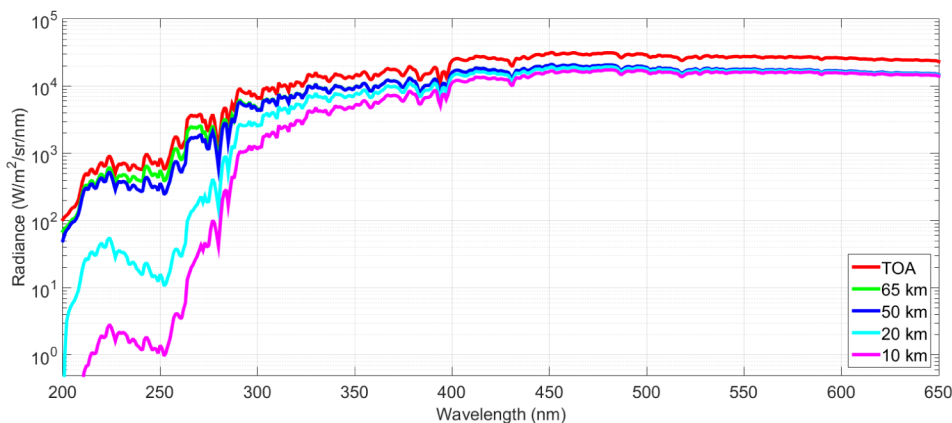


Fig. 4. Solar radiances used for the analysis of the UVIS sensitivity corresponding to observations performed at the top of the atmosphere and at the tangent heights of 65, 50, 20 and 10km.

Performances of the solar occultation channel of UVIS have been computed for an integration time of 0.2s, considering a binning on a 8 pixels column. The operating temperature has been assumed to be 298K. The signal level is high and is the dominant contribution. Signal from the 2nd diffraction order can be neglected, as can be seen from Fig. 5 (Left panel). The readout noise is much smaller than the shot noise and the dark current

noise and is not represented in the figure. Finally, the SNR achieved in this configuration (0.2s integration, binning on 8 rows, no spectral binning) are shown in Fig. 5 (Right panel). They are also compared with SNR values obtained without any binning, which corresponds to a SNR roughly  $\sqrt{8}$  ( $\approx 2.8$ ) times lower since the SNR is shot noise limited. We can clearly see that the SNR follow the radiances, i.e. with the effect of the CO<sub>2</sub> absorption at the lower tangent heights at wavelength lower than 250nm as well as the absorption of O<sub>3</sub>. SNR > 1000 are easily reached for wavelengths higher than 300nm. Below this limit, SNR are limited by the attenuation due to the atmosphere itself, mainly CO<sub>2</sub> and O<sub>3</sub>.

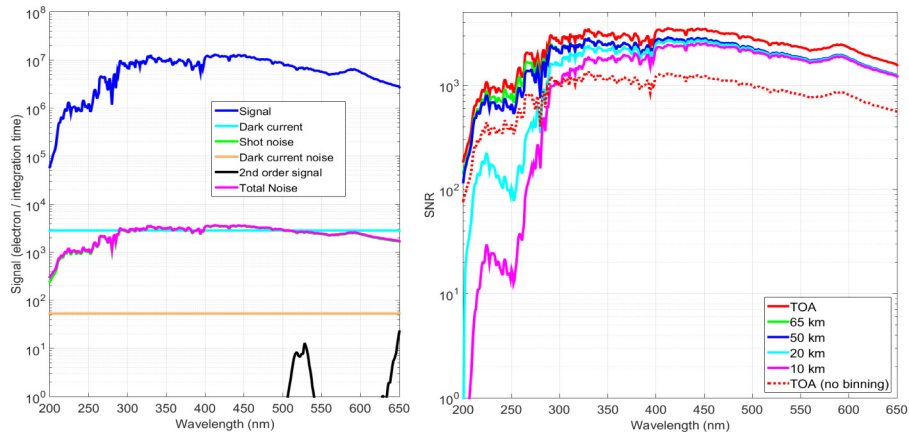


Fig. 5. (Left) Number of counts for the UVIS solar occultation channel corresponding to an observation at top of the atmosphere (no atmospheric attenuation). (Right) SNR as a function of the wavelength for the UVIS channel operating in solar occultation mode: for an observation at the top of the atmosphere when no binning is considered (dotted red line: SNR for one single line), when binning on 8 lines is considered (red line), and for observations corresponding to tangent heights of 65, 50, 20, and 10km (with binning).

#### 4.2 Nadir observations

For nadir observations, several scenarios have been considered to be representative of different observation conditions at Mars. They correspond to combinations of the following conditions: two different Sun-Mars distances (aphelion and perihelion); three different albedos (bright spots, dark areas, average), and then either different solar zenith angles or different aerosols loadings (different values of optical depth). Table 2 summarizes the different parameters used for the simulation of the radiances. In total, 48 radiances have been obtained and used as input for the SNR model. The surface is modelled using the Hapke formalism [18], considering the wavelength dependence based on the surface characteristics in the UV from [19] and in the visible from [20]. Table 2 indicates the values of the Hapke parameter at 320nm for the different types of surface considered in this study. The radiances have been simulated using a full scattering scheme that has already been adapted to Mars conditions [21–23]. These include the Rayleigh scattering, but no atmospheric absorption. Aerosols properties are wavelength dependent and are from [19] and [24] for the UV and visible spectral regions respectively. The Sun irradiance is the same as the one considered in Section 4.1. The radiances are shown in Fig. 6. As can be seen, they cover a wide range of values that would be encountered during the ExoMars mission.

Since the incoming light level is low, integration time has been set to its maximum value (15s). The signal is accumulated over 64 rows, which correspond to all the rows that actually collect the signal. The operating detector temperature has been assumed to be 298K. The different electron counts are presented in Fig. 7 for one scenario (perihelion, bright spot,  $\text{sza} = 45^\circ$ ,  $\tau = 0.1$ ), showing the signal, dark current, shot noise, dark current noise and overall noise. It is worth noting that the dark current is much higher than the overall noise and of the

same order of magnitude as the signal, even higher than the signal at wavelengths below 250nm. Hence, a very accurate estimation of the dark current is crucial and will be monitored cautiously during the entire mission.

**Table 2. Different conditions considered for the simulation of incoming radiation for the nadir UVIS observations**

Scenario	Aphelion	Perihelion
$L_S$	71°	251°
$R_{p-s}$	1.67AU	1.38AU
Albedo	Hapke parameter at 320nm	
Bright spots	0.12	
Dark areas	0.06	
Average	0.095	
Dust impact	sza = 45°	
	$\tau = 0.1, 0.4, 0.7, \text{ and } 1.0$	
sza impact	AOD = 0.2	
	sza = 0°, 45°, 65°, 80°	

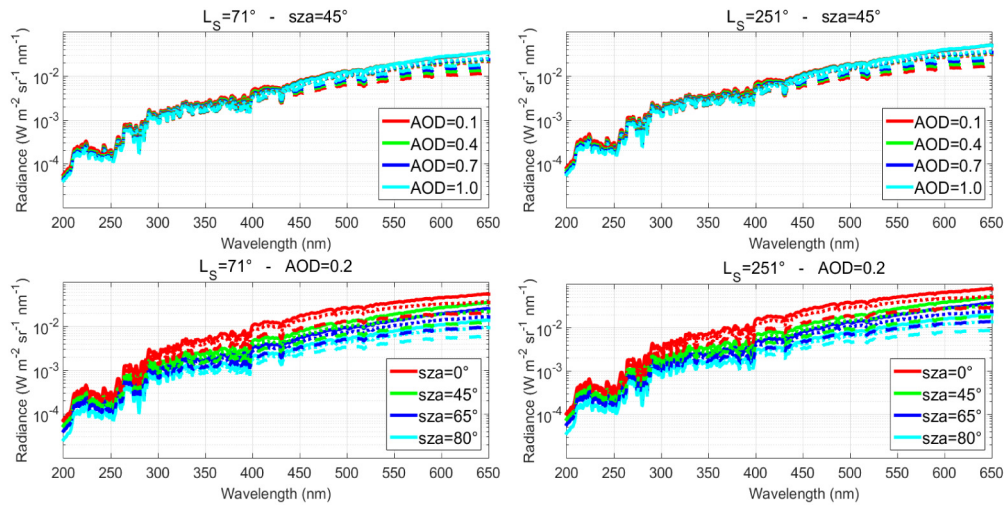


Fig. 6. Radiances used as input for the SNR sensitivity study. They correspond to two different Sun-Mars distances (aphelion, left column and perihelion, right column) and for different aerosol loadings (top panels) and different solar zenith angles (bottom panels). Solid, dotted and dashed lines correspond to the different albedos (bright spots, average, and dark areas) respectively.

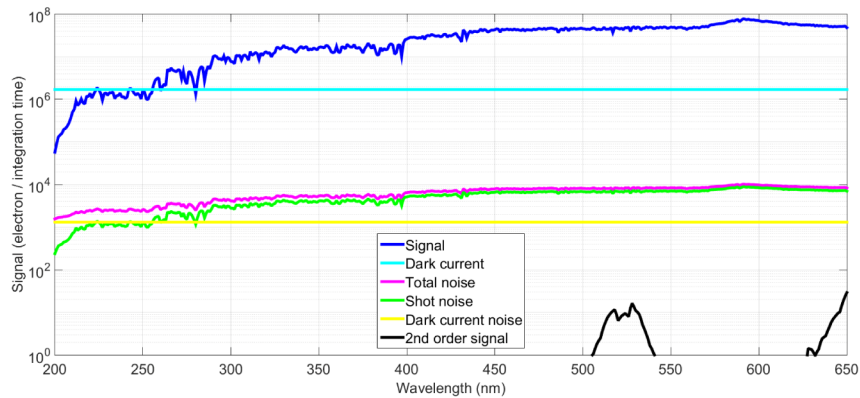


Fig. 7. Signal counts for the nadir channel for a typical nadir scenario.

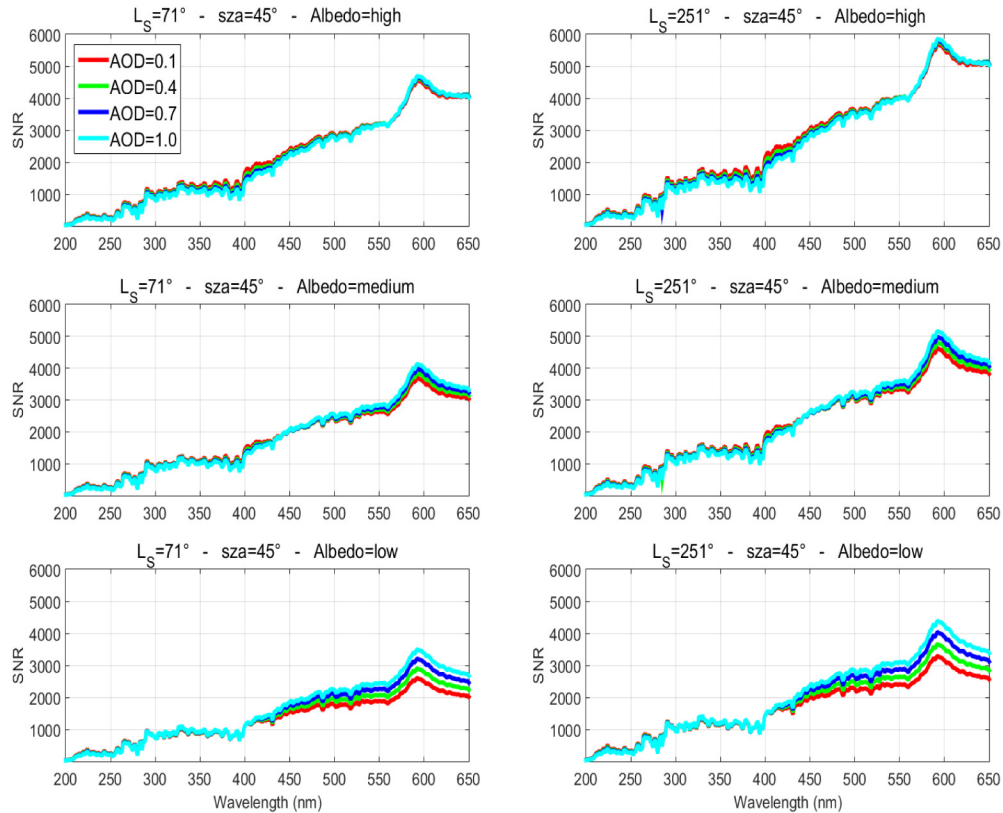


Fig. 8. Impact of the dust loading on the signal to noise-to-ratio of the UVIS nadir channel. The plots correspond to two different Sun-Mars distances (aphelion, left column and perihelion, right column) and for different albedos (bright spots- top panels, average – central panels, and dark areas – bottom panels). The different aerosol loadings are indicated by the color.

The signal-to-noise ratio has been computed for the different scenarios that were considered and are presented in Fig. 8 and Fig. 9 to illustrate the impact of the aerosol loading and the solar zenith angle respectively. For both figures, plots on the left correspond to the aphelion and on the right to the perihelion, thus for two different Sun-Mars distances. Obviously, when Mars is closer to the Sun, the radiation level is higher and the SNR is higher. This is also due to the fact that an important contribution to the noise comes from the dark current which does not depend on the incoming signal. Another obvious consideration is the effect of the surface albedo (best seen in Fig. 9): when higher, thus when the reflectance is larger, the signal is higher, and again the SNR is higher. The effect of the aerosol optical depth is enhanced when the surface is darker (bottom panels of Fig. 8). The increase of signal (and SNR) for increasing optical depth is explained by the properties of the aerosol included in the simulations [24]: the single scattering albedo at 400nm and 670nm is 0.63 and 0.93 respectively, leading to more scattering at higher wavelengths. For higher dust levels, the contribution of the scattering will increase. Also as expected, SNR are lower for high solar zenith angles. From these figures, we can see that SNR easily reach values above 1000 for wavelengths higher than 300nm, and for almost all Martian conditions. SNR even reach values higher than 5000 in the visible part of the spectrum. However, as expected, SNR values for wavelengths lower than 300nm are lower. In this spectral region the signal and SNR are low because primarily of the low radiation level emitted by the Sun, on top of which absorption by CO<sub>2</sub> and O<sub>3</sub> (not shown) further decrease the signal. One solution would be to bin also spectrally, thus artificially reducing the resolution of the instrument and increasing

the SNR. This could be done since the absorption features of O<sub>3</sub> (and other species absorbing in the UV-visible range) are large.

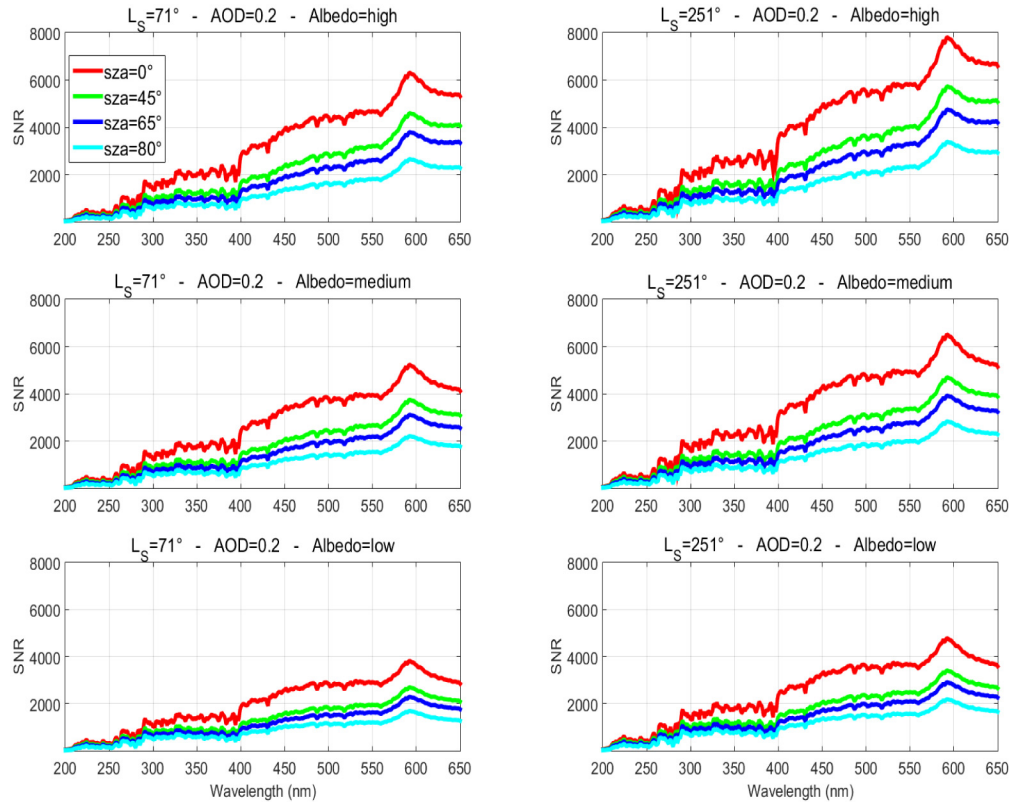


Fig. 9. Impact of the solar zenith angle on the signal to noise-to-ratio of the UVIS nadir channel. The plots correspond to two different Sun-Mars distances (aphelion, left column and perihelion, right column) and for different albedos (bright spots- top panels, average – central panels, and dark areas – bottom panels). The different solar zenith angles are indicated by the color.

## 5. Conclusions

NOMAD is a spectrometer suite that will be part of the ExoMars mission towards Mars [1]. It will be composed of three channels, operating in the UV, visible and IR spectral ranges and performing solar occultation and nadir observations [2, 3].

SNR > 1000 are easily reached for wavelengths higher than 300nm. Below this limit, SNR are limited by the lower solar radiation and the attenuation due to the atmosphere itself, mainly CO<sub>2</sub> and O<sub>3</sub>. Binning is one standard method used to increase the SNR. In this study, we only investigated the binning of rows, not the spectral binning which would also be possible with the UVIS channel. This would not be the preferred option, because it would obviously reduce the spectral resolution. We have also shown that removal of the dark current is crucial and should be done very accurately. Indeed, the dark current will be monitored during the complete mission by performing devoted dark sky observations. However, the easiest and most practical solution would be to record a dark frame before or after each Mars measurements. In that case, we are sure that the dark current is completely removed and corresponds to exactly the same recording conditions.

Although the analysis has been carried out on the latest version of the SNR models of the UVIS channel, containing the updated characteristics of the optical elements, this remains a theoretical exercise that will be re-evaluated when calibration data will be available, either

after the analysis and interpretation of the measurement made in the laboratory just before delivery of the instrument to the spacecraft industry, or in-flight. The true performances will however not be revealed until the first Martian measurements are performed.

In the companion to this paper we will investigate the SNR achieved by the two IR channels, SO and LNO, of the NOMAD instrument [6].

### Acknowledgments

The NOMAD instrument is led by the Belgian Institute for Space Aeronomy (IASB-BIRA, Brussels), assisted by Co-PI teams from Spain (IAA/CSIC, Granada), Italy (IAPS/INAF, Rome) and the United Kingdom (Open University, Milton-Keynes). Associated teams contributing to the design and development of NOMAD were CSL (Liège, Belgium) and IDR-UPM (Madrid, Spain). We thank all engineering and supporting personnel in these teams. Several industrial partners were associated to the abovementioned teams. The industrial efforts were coordinated by a Belgian prime contractor (OIP, Oudenaarde). The UVIS channel has been developed at Lambda-X (Nivelles, Belgium).

NOMAD has been made possible thanks to funding by the Belgian Science Policy Office (BELSPO) and financial and contractual coordination by the ESA Prodex Office (contracts n° 4000107727 and 4000103401). The research was performed as part of the “Interuniversity Attraction Poles” programme financed by the Belgian government (Planet TOPERS, contract PAI n° P7/15). UK funding is acknowledged under the UK Space Agency grant ST/I003061/1.

<sup>†</sup>**The NOMAD Team – Science Team:** Vandaele A.C.; Lopez Moreno J.J.; Bellucci G.; Patel M.; Allen M.; Altieri F.; Aoki S.; Bolsée D.; Clancy T.; Cloutis E.; Daerden, F.; Depiesse C.; Fedorova A.; Formisano V.; Funke B.; Fussen D.; Garcia-Comas M.; Geminale A.; Gérard J.-C.; Gillotay D.; Giuranna M.; Gonzalez-Galindo F.; Ignatiev N.; Kaminski J.; Karatekin O.; Kasaba, Y.; Lefèvre F.; Lewis, S.; López-Puertas M.; López-Valverde M.; Mahieux A.; Mason J.; Mumma M.; Neary L.; Neefs E.; Novak, R.; Renotte E.; Robert S.; Sindoni G.; Smith M.; Thomas I.R.; Trokhimovskiy A.; Vander Auwera J.; Villanueva G.; Viscardy, S.; Whiteway J.; Willame Y.; Wilquet V.; Wolff M. - **Tech Team:** Alonso-Rodrigo G.; Aparicio del Moral B.; Barzin P.; BenMoussa A.; Berkenbosch S.; Biondi D.; Bonnewijn S.; Candini G.; Clairquin R.; Cubas J.; Delanoye S.; Giordanengo B.; Gissot S.; Gomez A.; Zafra J.-J.; Leese M.; Maes J.; Mazy E.; Mazzoli A.; Meseguer J.; Morales R.; Orban A.; Pastor-Morales M.; Perez-Grande I.; Ristic B.; Rodriguez-Gomez J.; Saggin B.; Samain V.; Sanz Andres A.; Sanz R.; Simar J.-F.; Thibert T.